Structural stability of REE-PO_4 (REE=Sm,Tb) under swift heavy ion irradiation

Cale Overstreet[a], Jacob Cooper[a], Eric O'Quinn[a], William Cureton[a], Raul Palomares[a], Julia Leys[b,c], Guido Deissmann[b], Stefan Neumeier[b], Chien-Hung Chen[d], Maik Lang[a*]

[a]*Department of Nuclear Engineering, University of Tennessee, Knoxville, Tennessee 37996, USA*
[b]*Forschungszentrum Jülich GmbH, Institute of Energy and Climate Research (IEK-6): Nuclear Waste Management and Reactor Safety, 52425 Jülich, Germany*
[c]*Karlsruhe Institute of Technology, Institute for Applied Materials (IAM-ESS), 76021 Karlsruhe, Germany*
[d]*Department of Geological Sciences, Stanford University, Stanford, California 94305, USA*

*Corresponding Author: mlang2@utk.edu

Keywords: REE-phosphates, monazite, xenotime, nuclear waste form, ion irradiation, X-ray diffraction, Raman spectroscopy, crystalline-to-amorphous transformation

Abstract

Rare earth element (REE) phosphates are an attractive host matrix for long-lived radionuclides from nuclear waste because of the radiation tolerance exhibited by naturally occurring REE phosphate specimens. Here we show that $SmPO_4$ (monazite structure) and $TbPO_4$ (xenotime structure) exhibit a similar amorphization response to swift heavy ion irradiation despite different starting structures. $SmPO_4$ and $TbPO_4$ were irradiated with 1.1 GeV Au ions and analyzed using synchrotron-based X-ray diffraction (XRD), Raman spectroscopy, and transmission electron microscopy (TEM). The radiation response of the phosphates was evaluated by extracting the amorphous fraction at each irradiation fluence, and a single-impact model was used to determine the amorphous cross section and track diameter. Amorphization within individual ion tracks was confirmed using head-on TEM imaging, and the amorphous track size agreed with the value deduced by XRD analysis. Raman measurements were performed to qualitatively confirm the ion-induced crystalline-to-amorphous transformation which proceeds similarly for both phosphates.

1. Introduction

Rare earth element (REE) phosphates, $REEPO_4$, have attracted much attention in recent years because of their potential to act as host matrices for encapsulating long-lived radionuclides from nuclear waste streams [1-7] . REE phosphates are naturally occurring minerals that can incorporate significant amounts of uranium and thorium. Natural specimens have been shown to structurally resist the effects from self-irradiation over long

periods of time [4, 7, 8], suggesting that synthetic analogues can be tailored to exhibit similar enhanced radiation tolerance [9, 10].

REE phosphates crystallize into two main structural families, monazite and xenotime. Lighter REE phosphates (e.g., REE = Sm) form the monazite structure, while the heavier REE phosphates (e.g., REE = Tb) adopt the xenotime structure [11-13]. Monazite crystallizes in a monoclinic system with space group $P2_1/n$ (Z=4), while the xenotime structure, characteristic of the mineral zircon, is tetragonal with space group $I4_1/amd$ (Z=4) [13]. Previous high-pressure studies have shown that the structural response of REE phosphates under compression depends strongly on the structure type, with the xenotime and monazite phases remaining stable up to 10 GPa and 40 GPa, respectively [14]. X-ray diffraction experiments on the monazite phase at high pressure have shown a linear decrease in lattice parameters and peak broadening with increasing pressure.

Radiation effects studies of the two structure types are much less common than high-pressure investigations [15, 16] with swift heavy ion studies being even less common. The primary source of radiation damage in an actinide-bearing waste form is from alpha decay, which produces an energetic alpha particle (~4 to 6 MeV) and a low-energy heavy recoil nucleus (50 – 180 keV) [17]. These two projectiles are representative of the two very different types of ion-matter interactions that occur depending on the kinetic energy. The low energy recoil ion directly displaces atoms from their lattice sites *via* ballistic collisions (nuclear energy loss). In contrast, the energetic alpha particle transfers its energy to the electrons of the target material, inducing electronic excitation and ionization, initiating a cascade of secondary electrons that quickly spreads radially (electronic energy loss). The electronic energy loss regime, characteristic of alpha particle exposure, is isolated using

projectiles produced experimentally at ion accelerator facilities; such "swift heavy ions" typically have GeV energies and penetrate on the order of tens of micrometers into their targets [18]. The resulting extremely high energy densities (up to tens of eV/atom) produce a confined, plasma-like state in the target material, which is dissipated through electron-phonon coupling to the lattice [19]. This energy transfer results in complex structural modifications within a highly localized nanoscale region, the so-called "ion track". In many ceramics, this cylindrical damage zone consists of an amorphous phase. While swift heavy ions have only limited relevance for radioactive waste forms, their large penetration depths allow for advanced bulk characterization, such as synchrotron-based XRD [20] and neutron total scattering [21]. Previous irradiation studies of REE phosphates focused on the monazite-structure family and revealed that Au ions with energies of 1.5 MeV induce amorphization at high fluences (~1×10^{14}) [7]. In contrast, there is little information available on the behavior of the xenotime phase under energetic ion irradiation [16, 22]. Thus, the influence of the starting structure on the radiation response of this important class of materials is currently not understood. The behavior under high pressure suggests a significantly different stability among the two structure types.

The aim of this study is to investigate how the two REE phosphate structure types behave under swift heavy ion irradiation with predominantly electronic energy loss. Monazite ($SmPO_4$) and xenotime ($TbPO_4$) phases were irradiated with swift heavy ions and analyzed by means of synchrotron-based XRD, Raman spectroscopy, and high-resolution TEM. The two neighboring chemical compositions have been chosen to minimize the effect of cation size (if any) on the observed radiation behavior.

2. Experimental

2.1 Sample Synthesis

Two REE phosphate samples, $SmPO_4$ and $TbPO_4$, were synthesized at ambient temperature *via* a coprecipitation route [5]. Aqueous lanthanide (Ln = Tb, Sm) nitrate solutions were mixed with citric acid (CA) solution as a chelating agent in a molar ratio of Ln:CA = 1:2. Subsequently, an excess of phosphoric acid (P) was added (Ln:P = 1:5). To obtain a complete precipitation, the pH was adjusted to ~10 using 25% $NH_4(OH)$ while stirring. After drying at 90°C, the precipitates were calcined (550°C, 3 h) and sintered (1600°C, 5 h). The samples were ground within an agate mortar after each thermal treatment step. The chemical purity of both samples was verified *via* energy dispersive X-ray spectroscopic analysis on pellet samples, using a scanning electron microscope (Quanta 200F, FEI) equipped with an Apollo X silicon drift Detector (EDAX).

2.2 Ion Irradiation

Microcrystalline (1-5 µm) powders of $SmPO_4$ and $TbPO_4$ were irradiated with swift heavy ions using sample holders designed to allow ions to completely penetrate and deposit near-constant electronic energy loss, dE/dx, through the entire thickness [23]. The samples were uniaxially pressed into several holes with a diameter of ~100 µm drilled into 50-µm thin molybdenum foils. Details on the sample holders and the sample preparation method for ion irradiation are provided elsewhere [24].

The irradiation experiment was performed in vacuum and at ambient temperatures at the M1 beamline of the UNILAC linear accelerator at the GSI Helmholtz Centre for Heavy Ion Research in Darmstadt, Germany using 1.1 GeV ^{197}Au ions. The various sample holders were irradiated to 10 different ion fluences, ranging from 2×10^{11} - 8×10^{12} ions/cm^2.

Each holder contained samples of both $SmPO_4$ and $TbPO_4$, ensuring that both samples were irradiated under identical beam conditions. This reduced the relative fluence uncertainty and enabled precise comparison of the radiation responses between the two sample types.

The ion range and dE/dx value was calculated for both sample types using the SRIM 2008 code [25]. Based on previous sample preparation using the same holder system and actinide oxide powders, the actual sample density was assumed to be on the order of 60% of the theoretical value [26]. The ion range was accordingly adjusted and the SRIM data scaled according to a procedure described in detail elsewhere [23]. The dE/dx evolution for both samples is shown in Figure 1 as a function of density-corrected penetration depth. It is apparent that the ions completely penetrated the samples and deposited a median electronic energy loss of 34 ± 1 keV/nm for both $SmPO_4$ and $TbPO_4$. There is variation in the electronic energy loss across the range of the ion because of sample thickness; however, the nuclear energy loss is at least an order of magnitude smaller across the entire ion path within the sample and is therefore neglected in this study.

2.3 Characterization

Synchrotron X-ray diffraction (XRD) was used to examine the two phosphate structure types after irradiation in order to characterize the induced radiation damage. XRD experiments were performed at the High-Pressure Collaborative Access Team (HPCAT) 16-BM-D beamline of the Advanced Photon Source (APS) at Argonne National Laboratory. Data were collected in transmission mode on a 2D Mar345 image plate detector using a monochromatic photon beam of 29.2 keV (λ = 0.4246 Å). One-dimensional patterns were produced by integrating the diffraction images using the

software Dioptas [27]. The detector was calibrated using a NIST powder CeO_2 standard, and amorphous phase fractions were quantified using a peak-deconvolution procedure based on the Fityk and AMORPH programs [28, 29]. Details of the synchrotron-based XRD measurements and analysis of XRD patterns with respect to amorphous sample fractions are described elsewhere [24, 30].

TEM analysis was conducted at Stanford University on a FEI Tecnai G2 F20 X-TWIN transmission electron microscope with an operating voltage of 200 keV. TEM samples were prepared by collecting small, crushed phosphate grains on a carbon film supported by a molybdenum grid. High-resolution images were recorded in top-view mode, with the electron beam being parallel to the ion track, to analyze the size and morphology of ion tracks.

Raman spectroscopy was also performed on the irradiated samples in order to complement the XRD data and evaluate the effects of swift heavy ion irradiation on local atomic arrangements. Raman measurements were performed using a Horiba LabRAM HR Evolution instrument equipped with a 785 nm excitation laser source and a liquid-nitrogen cooled charge coupled device (CCD) detector. Raman data were collected with a long working distance objective and the laser power was limited to 50 mW to avoid undesired annealing of radiation damage. Reported spectra represent the average of 3 measurements performed on different sample locations.

3. Results and Discussion

$SmPO_4$ and $TbPO_4$ were characterized before and after irradiation to different ion fluences with synchrotron XRD to assess structural changes induced by the 1.1 GeV Au

ions (Figure 2). The data show that both materials are crystalline prior to irradiation, as indicated by the sharp diffraction maxima. Indexing of the Bragg peaks confirms that $SmPO_4$ exhibits the monazite structure and $TbPO_4$ exhibits the xenotime structure. Both samples are fully crystalline and phase-pure with no detectable impurity concentrations. After irradiation, all crystalline peaks begin to broaden and decrease in intensity. The loss of Bragg peak intensity is accompanied by the appearance of broad, diffuse bands, which indicates that both materials gradually amorphize with increasing ion fluences.

Diffuse scattering bands centered at ~1.5 and ~2.0 $Å^{-1}$ appear in the diffraction patterns of both materials at around 5×10^{11} to 1×10^{12} ions/cm^2. All crystalline diffraction maxima of $SmPO_4$ are for the most part absent in the XRD patterns after irradiation to 3×10^{12} ions/cm^2, which is evidence of complete amorphization and loss of long-range structure in this compound. $SmPO_4$ remains fully amorphous at higher fluences, and no irradiation-induced recrystallization is observed. Amorphous bands are most evident for $TbPO_4$ after irradiation to 3×10^{12} ions/cm^2, and all crystalline diffraction maxima are fully absent at 5×10^{12} ions/cm^2. $TbPO_4$, like $SmPO_4$, shows no indication of recrystallization up to the maximum fluence of 8×10^{12} ions/cm^2.

To better compare the amorphization behavior of both samples and elucidate the damage accumulation mechanism, amorphous fractions were determined at each fluence. This was completed by first analyzing the area beneath diffuse scattering bands with Gaussian peak fitting after peak-deconvolution. Peak areas attributed to amorphous bands were normalized to the total peak area (integrated peak intensity) in the patterns, which included both Bragg (i.e., crystalline phase) and amorphous peaks. The uncertainty in this process was estimated by repeatedly fitting each diffraction pattern, which yielded error

bars in amorphous phase fractions representing the standard error of mean values. This procedure is identical to the method outlined by Lang *et al.* [30]. Relative changes in amorphous phase fractions for $SmPO_4$ and $TbPO_4$ with increasing ion fluence are shown in Figure 3. Both samples amorphize at a similar rate with respect to ion fluence and become fully amorphous at the maximum fluence of 8×10^{12} ions/cm^2. The increase in amorphous phase fraction as a function of increasing fluence shows the characteristic behavior of a single-impact damage accumulation model [31]. The single-impact model in this case assumes that each ion-matter interaction results in a cylindrical amorphous damage region, the so-called "ion track". At lower fluences, ion tracks are well separated, and the amorphous phase production is linearly proportional to fluence. Upon further irradiation, amorphous phase production saturates at high fluences when ion tracks overlap. Numerical fitting to the data displayed in Figure 3 (solid lines) with a Poisson-type function enables to deduce the cross-sectional areas of the amorphous ion tracks:

$$f_a(\phi) = f_{sat}(1 - e^{-\sigma\phi}) \qquad (1)$$

where σ is the amorphization cross-section, f_a is the amorphous fraction, f_{sat} is the saturation value for the amorphous fraction (here 1.0 or 100%), and ϕ is the ion fluence [32]. By assuming cylindrical ion tracks, diameters were calculated from σ to be 8.0±0.6 nm and 7.7±0.5 nm for $SmPO_4$ and $TbPO_4$, respectively. Thus, 1.1 GeV Au ions produce amorphous ion tracks of the same size in both materials, independent of the different starting structures.

To independently assess track formation and associated amorphization, samples irradiated to a low fluence were analyzed by TEM in cross-sectional view (Figure 4). The TEM images clearly display ion tracks in both materials, which are apparent by their

distinct contrast change with respect to the surrounding matrix. Selected area diffraction (SED) confirmed that the tracks are amorphous in both materials. Since the samples were polycrystalline powders, the orientation of ion tracks (direction of impinging ions with respect to sample surface) was random and not along specific crystallographic directions; the boundary between the amorphous track and crystalline matrix is therefore less pronounced. However, the quality of the TEM images is sufficient to estimate the ion track size reasonably well in both materials, yielding diameters in $SmPO_4$ and $TbPO_4$ of 8 nm for both samples. These values are in close agreement with the diameters determined by the XRD pattern analysis of amorphous fractions and single-impact model fits.

In addition to XRD and TEM, Raman spectroscopy measurements were performed on the irradiated $SmPO_4$ and $TbPO_4$ samples to characterize changes in local atomic arrangements. Figure 5 shows selected Raman spectra of both materials before and after irradiation with increasing ion fluence. The Raman spectra of pristine $SmPO_4$ and $TbPO_4$ exhibit different modes in accordance with their different crystal structures, which agrees well with previously reported Raman data of xenotime and monazite compounds [33]. The most intense bands located at ~1000 and 1100 cm^{-1} were attributed to the symmetrical (υ_1) and antisymmetrical (υ_3) stretching vibrational modes of the PO_4 polyhedra, respectively. The Raman spectra of $SmPO_4$ appear to be almost unaffected until irradiation to a fluence of ~1×10^{12} ions/cm^2, when amorphization becomes apparent. Amorphization is indicated in the Raman spectra by the increase of background intensity accompanied by a decreasing intensity of crystalline peaks, which is attributed to accumulated atomic disorder from irradiation. At higher fluences, most sharp Raman peaks are absent, except three broad peaks that persists up to the maximum fluences for $SmPO_4$. These broad bands are

attributed to the four normal modes (υ_1- υ_4) of the PO_4 polyhedron in the sample, indicating that these structural units remain largely intact after irradiation. This agrees with data collected by Picot *et al.* [34, 35], which also showed that the monazite structure amorphizes after irradiation, yet the modes belonging to the PO_4 polyhedra were still present. However, they used 7 MeV Au ion irradiation with limited penetration depth, and undamaged samples layers beyond the ion range may still contribute to their Raman spectra [35]. The overall trend with increasing fluence applies equally to the $TbPO_4$ Raman spectra. However, amorphization appears in the spectra at slightly lower fluences compared to the monazite phosphate (7×10^{11} instead of 1×10^{12} ions/cm^2) and the two stretching modes of the PO_4 structural units are no longer clearly observable above a fluence of 1.5×10^{12} ions/cm^2. These peaks are only vaguely evident above the background at higher fluences, which may be related to much more distorted PO_4 polyhedra in the $TbPO_4$ sample.

Complementary characterization reveals a consistent radiation response of monazite and xenotime phosphate families under swift heavy ion irradiation at room temperature. Both rare-earth element phosphate structure types gradually amorphize at similar fluence rates, and the data show both materials become completely amorphous above a comparable fluence. Amorphization behavior of these materials is well described assuming a single-impact model for damage accumulation. This indicates that each swift heavy ion produces a fully amorphous cylindrical ion track, and both bulk materials exhibit full loss of long-range atomic ordering. High-resolution TEM images confirm the formation of individual amorphous ion tracks with no apparent disordered shell as reported for many complex oxides [21]. Raman spectra show that PO_4 tetrahedra persist in both materials throughout the crystalline-to-amorphous transition, implying that changes to their

connectivity induced by the irradiation are responsible for the loss of long-range coherency. These structural units show a more pronounced fingerprint in the Raman spectra of amorphous $SmPO_4$ as compared with $TbPO_4$, which could indicate small variations in the local atomic arrangement of both materials. Additional short-range characterization, such as neutron total scattering, is needed to gain further insight into the short-range behavior during the amorphization process.

The results of this study show that the starting structure of the phosphate material has little to no influence on the size of ion tracks. This agrees well with data compiled in a recent review article that compared track diameters in a wide range of complex ceramics irradiated with swift heavy ions of kinetic energy between 5 and 10 MeV/u [36]. While the track morphology can be complex for different materials with a number of concentric damage zones (e.g., core-shell morphology), the overall track size is surprisingly similar, despite different chemical compositions and starting structures. This was explained by the highly transient energy depositions within the track region that result in nanometer-sized thermal-spike zones. The track diameter is mostly affected by this initial energy deposition, which is similar in many insulators for a given energy loss and independent of chemical composition and starting structure [36]. Recovery processes during track quenching are probably more sensitive to target material properties and result in distinct damage morphologies in different complex ceramics.

Findings from this study differ from high-temperature ion irradiation studies using low-energy ions, which show that the monazite structure is less susceptible to amorphization compared with xenotime-structured REE phosphates [15]. This temperature dependence is typically attributed to point defect mobility and was partially explained by

differences in electronic-to-nuclear stopping power (ENSP) ratios in the materials [15]. It was shown that xenotime-type structures exhibit higher critical temperatures (T_c), and thus have higher amorphization susceptibility, compared with monazite-type REE phosphate structures at identical ESNP ratios. However, in the present study, we show that amorphization susceptibility for xenotime and monazite structures is very similar, which is likely attributable to the extremely high ENSP ratio yielded by swift heavy ion irradiation. Future studies should aim to elucidate differences in amorphization susceptibility between xenotime and monazite structures throughout a broad range of ENSP ratios.

In contrast to swift heavy ion irradiation, xenotime- and monazite-structured REE phosphates show a divergent response to high-pressure exposure [37]. TbPO4 xenotime was found to transform into the monazite structure above 10 GPa, while SmPO4 monazite retains its starting structure when being compressed over the same pressure range. Thus, the resistance to high pressure more closely resembles the behavior under low-energy ion irradiation at high temperature [15]. Together with the data of the present study, this shows that material performance and structural stability under extreme conditions is complex and depends on the type of regime that is considered.

4. Conclusion

Monazite-type $SmPO_4$ and xenotime-type $TbPO_4$ were studied under swift heavy ion irradiation by a complementary analytical approach. Both structures undergo amorphization at similar rates with increasing fluence due to accumulation of amorphous ion tracks of similar size. Raman spectroscopy shows that the local structure of the amorphous phase is retained in both materials' PO_4 polyhedra independently of the loss of

long-range crystallinity. The similarity in radiation response of $SmPO_4$ and $TbPO_4$ can be attributed to the extremely high electronic-to-nuclear stopping power ratio induced by the 1.1 GeV Au ions and the associated transient energy depositions. These results suggest that changes in the chemistry, like in nuclear waste forms, and in the structure will not greatly affect the overall radiation response of REE phosphate materials to highly energetic ions.

Acknowledgements

This work was supported by the U.S. Department of Energy, Office of Science, Basic Energy Sciences, under Award DE-SC0020321. Synchrotron XRD measurements were performed at HPCAT (Sector 16), Advanced Photon Source (APS), Argonne National Laboratory. HPCAT operations are supported by DOE-NNSA's Office of Experimental Sciences. The Advanced Photon Source is a U.S. Department of Energy (DOE) Office of Science User Facility operated for the DOE Office of Science by Argonne National Laboratory under Contract No. DE-AC02-06CH11357. HPCAT beam time was provided by the Chicago/DOE Alliance Center. The results presented here are based on a UMAT experiment, which was performed at the M-branch-beamline of the UNILAC at the GSI Helmholtzzentrum für Schwerionenforschung, Darmstadt (Germany) in the frame of FAIR Phase-0. C.O. acknowledges support from the Center for Materials Processing (CMP) at the University of Tennessee, Knoxville.

References

1. Begun G. M., Beall G. W., Boatner L. A., Gregot W. J., *Raman spectra of the rare earth orthophosphates.* Journal of Raman Spectroscopy, 1981. **11**(4).
2. Lutze, Werner and Rodney C Ewing, *Radioactive waste forms for the future.* 1988.
3. Ewing, Rodney C and LuMin Wang, *Phosphates as nuclear waste forms.* Reviews in mineralogy and geochemistry, 2002. **48**(1): p. 673-699.
4. Ruschel, Katja, Lutz Nasdala, Andreas Kronz, John M Hanchar, Daniel M Többens, Radek Škoda, Friedrich Finger, and Andreas Möller, *A Raman spectroscopic study on the structural disorder of monazite–(Ce).* Mineralogy and Petrology, 2012. **105**(1): p. 41-55.
5. Dacheux, Nicolas, Nicolas Clavier, and Renaud Podor, *Monazite as a promising long-term radioactive waste matrix: Benefits of high-structural flexibility and chemical durability.* Am. Mineral, 2013. **98**(5-6): p. 833-847.
6. Neumeier, Stefan, Yulia Arinicheva, Yaqi Ji, Julia M Heuser, Piotr M Kowalski, Philip Kegler, Hartmut Schlenz, Dirk Bosbach, and Guido Deissmann, *New insights into phosphate based materials for the immobilisation of actinides.* Radiochimica acta, 2017. **105**(11): p. 961-984.
7. Seydoux-Guillaume, A. M., X. Deschanels, C. Baumier, S. Neumeier, W. J. Weber, and S. Peuget, *Why natural monazite never becomes amorphous: Experimental evidence for alpha self-healing.* American Mineralogist, 2018. **103**(5): p. 824-827.
8. Gramaccioli, C. M. and T. V. Segalstad, *URANIUM-RICH AND THORIUM-RICH MONAZITE FROM A SOUTH-ALPINE PEGMATITE AT PIONA, ITALY.* American Mineralogist, 1978. **63**(7-8): p. 757-761.
9. Weber, William J, Rodney C Ewing, CRA Catlow, T Diaz De La Rubia, Linn W Hobbs, C Kinoshita, AT Motta, M Nastasi, EKH Salje, and ER Vance, *Radiation effects in crystalline ceramics for the immobilization of high-level nuclear waste and plutonium.* Journal of Materials Research, 1998. **13**(6): p. 1434-1484.
10. Ewing, Rodney C, Alkiviathes Meldrum, LuMin Wang, and ShiXin Wang, *Radiation-induced amorphization.* Reviews in mineralogy and geochemistry, 2000. **39**(1): p. 319-361.
11. Gerhard Franz, Gerhard Andrehs, D. Rhede, *Crystal chemistry of monazite and xenotime from Saxothuringian-Moldanubian metapelites, NE Bavaria, Germany.* European Journal of Mineralogy, 1996. **8**.
12. Heinrich, W., G. Andrehs, and G. Franz, *Monazite-xenotime miscibility gap thermometry .1. An empirical calibration.* Journal of Metamorphic Geology, 1997. **15**(1): p. 3-16.
13. Ni, Yunxiang, John M Hughes, and Anthony N Mariano, *Crystal chemistry of the monazite and xenotime structures.* American Mineralogist, 1995. **80**(1-2): p. 21-26.

14. J.M. Heuser, R.I. Palomares, J.D. Bauer, M.J. Lozano Rodriguez, J. Cooper, M. Lang, A.C. Scheinost, H. Schlenz, B. Winkler, D. Bosbach, S. Neumeier, G. Deissmann, *Structural characterization of (Sm,Tb)PO4 solid solutions and pressure-induced phase transitions.* Journal of the European Ceramic Society, 2018. **38**(11): p. 4070-7081.
15. Meldrum, A., L. A. Boatner, and R. C. Ewing, *Displacive radiation effects in the monazite- and zircon-structure orthophosphates.* Physical Review B, 1997. **56**(21): p. 13805-13814.
16. Rafiuddin, Mohamed Ruwaid, Anne-Magali Seydoux-Guillaume, Xavier Deschanels, Adel Mesbah, Cedric Baumier, Stephanie Szenknect, and Nicolas Dacheux, *An in-situ electron microscopy study of dual ion-beam irradiated xenotime-type ErPO4.* Journal of Nuclear Materials, 2020. **539**: p. 152265.
17. Meldrum, A and DJ Cherniak, *Ion beams in the geological sciences*, in *Materials Science with Ion Beams*. 2009, Springer. p. 317-343.
18. Lang, Maik, Eric C O'Quinn, Jacob Shamblin, and Jörg Neuefeind, *Advanced Experimental Technique for Radiation Damage Effects in Nuclear Waste Forms: Neutron Total Scattering Analysis.* MRS Advances, 2018. **3**(31): p. 1735-1747.
19. Zhang, Jiaming, Maik Lang, Rodney C Ewing, Ram Devanathan, William J Weber, and Marcel Toulemonde, *Nanoscale phase transitions under extreme conditions within an ion track.* Journal of Materials Research, 2010. **25**(7): p. 1344-1351.
20. Lang, Maik, Fuxiang Zhang, Jiaming Zhang, Jianwei Wang, Jie Lian, William J Weber, Beatrice Schuster, Christina Trautmann, R Neumann, and Rodney C Ewing, *Review of A2B2O7 pyrochlore response to irradiation and pressure.* Nuclear Instruments and Methods in Physics Research Section B: Beam Interactions with Materials and Atoms, 2010. **268**(19): p. 2951-2959.
21. O'Quinn, Eric C, Cameron L Tracy, William F Cureton, Ritesh Sachan, Joerg C Neuefeind, Christina Trautmann, and Maik K Lang, *Multi-scale investigation of heterogeneous swift heavy ion tracks in stannate pyrochlore.* Journal of Materials Chemistry A, 2021. **9**(31): p. 16982-16997.
22. Lenz, Christoph, Gordon Thorogood, Robert Aughterson, Mihail Ionescu, Daniel J Gregg, Joel Davis, and Gregory R Lumpkin, *The quantification of radiation damage in orthophosphates using confocal μ-luminescence spectroscopy of Nd3+.* Frontiers in chemistry, 2019: p. 13.
23. Lang, M. I., F. X. Zhang, J. M. Zhang, C. L. Tracy, A. B. Cusick, J. VonEhr, Z. G. Chen, C. Trautmann, and R. C. Ewing, *Swift heavy ion-induced phase transformation in Gd2O3.* Nuclear Instruments & Methods in Physics Research Section B-Beam Interactions with Materials and Atoms, 2014. **326**: p. 121-125.
24. Lang, M., C. L. Tracy, R. I. Palomares, F. X. Zhang, D. Severin, M. Bender, C. Trautmann, C. Park, V. B. Prakapenka, V. A. Skuratov, and R. C. Ewing, *Characterization of ion-induced radiation effects in nuclear materials using synchrotron x-ray techniques.* Journal of Materials Research, 2015. **30**(9): p. 1366-1379.

25. Ziegler, J. F., M. D. Ziegler, and J. P. Biersack, *SRIM - The stopping and range of ions in matter (2010).* Nuclear Instruments & Methods in Physics Research Section B-Beam Interactions with Materials and Atoms, 2010. **268**(11-12): p. 1818-1823.
26. E. Luther, C. Necker, B. Mihaila, P. Papin, and D. Guidry, *Microstructural characterization of uranium oxide.* Trans. Am. Nucl. Soc. , 2011. **104**(257).
27. Prescher, Clemens and Vitali B Prakapenka, *DIOPTAS: a program for reduction of two-dimensional X-ray diffraction data and data exploration.* High Pressure Research, 2015. **35**(3): p. 223-230.
28. Wojdyr, Marcin, *Fityk: a general‐purpose peak fitting program.* Journal of Applied Crystallography, 2010. **43**(5‐1): p. 1126-1128.
29. Rowe, Michael C and Brendon J Brewer, *AMORPH: A statistical program for characterizing amorphous materials by X-ray diffraction.* Computers & geosciences, 2018. **120**: p. 21-31.
30. Lang, M., F. X. Zhang, R. C. Ewing, J. Lian, C. Trautmann, and Z. W. Wang, *Structural modifications of Gd(2)Zr(2-x)Ti(x)O(7) pyrochlore induced by swift heavy ions: Disordering and amorphization.* Journal of Materials Research, 2009. **24**(4): p. 1322-1334.
31. Weber, W. J., *Models and mechanisms of irradiation-induced amorphization in ceramics.* Nuclear Instruments & Methods in Physics Research Section B-Beam Interactions with Materials and Atoms, 2000. **166**: p. 98-106.
32. Gibbons, J. F., *ION IMPLANTATION IN SEMICONDUCTORS .2. DAMAGE PRODUCTION AND ANNEALING.* Proceedings of the Institute of Electrical and Electronics Engineers, 1972. **60**(9): p. 1062-&.
33. Stavrou, E., A. Tatsi, E. Salpea, Y. C. Boulmetis, A. G. Kontos, Y. S. Raptis, and C. Raptis. *Raman study of zircon-structured RPO4 (R = Y, Tb, Er, Tm) phosphates at high pressures*. in *21st AIRAPT/45th EHPRG International Conference on High Pressure Science and Technology*. 2007. Univ Catania, Dept Phys Astronomy, Catania, ITALY.
34. Picot, V., X. Deschanels, S. Peuget, B. Glorieux, A. M. Seydoux-Guillaume, and R. Wirth, *Ion beam radiation effects in monazite.* Journal of Nuclear Materials, 2008. **381**(3): p. 290-296.
35. Nasdala, Lutz, Rainer Grötzschel, Sylvio Probst, and Bernd Bleisteiner, *Irradiation damage in monazite-(Ce): an example to establish the limits of Raman confocality and depth resolution.* The Canadian Mineralogist, 2010. **48**(2): p. 351-359.
36. Lang, Maik, Ram Devanathan, Marcel Toulemonde, and Christina Trautmann, *Advances in understanding of swift heavy-ion tracks in complex ceramics.* Current Opinion in Solid State and Materials Science, 2015. **19**(1): p. 39-48.
37. Heuser, JM, RI Palomares, JD Bauer, MJ Lozano Rodriguez, J Cooper, M Lang, AC Scheinost, H Schlenz, B Winkler, and D Bosbach, *Structural characterization of (Sm, Tb) PO4 solid solutions and pressure-induced phase transitions.* Journal of the European Ceramic Society, 2018. **38**(11): p. 4070-4081.

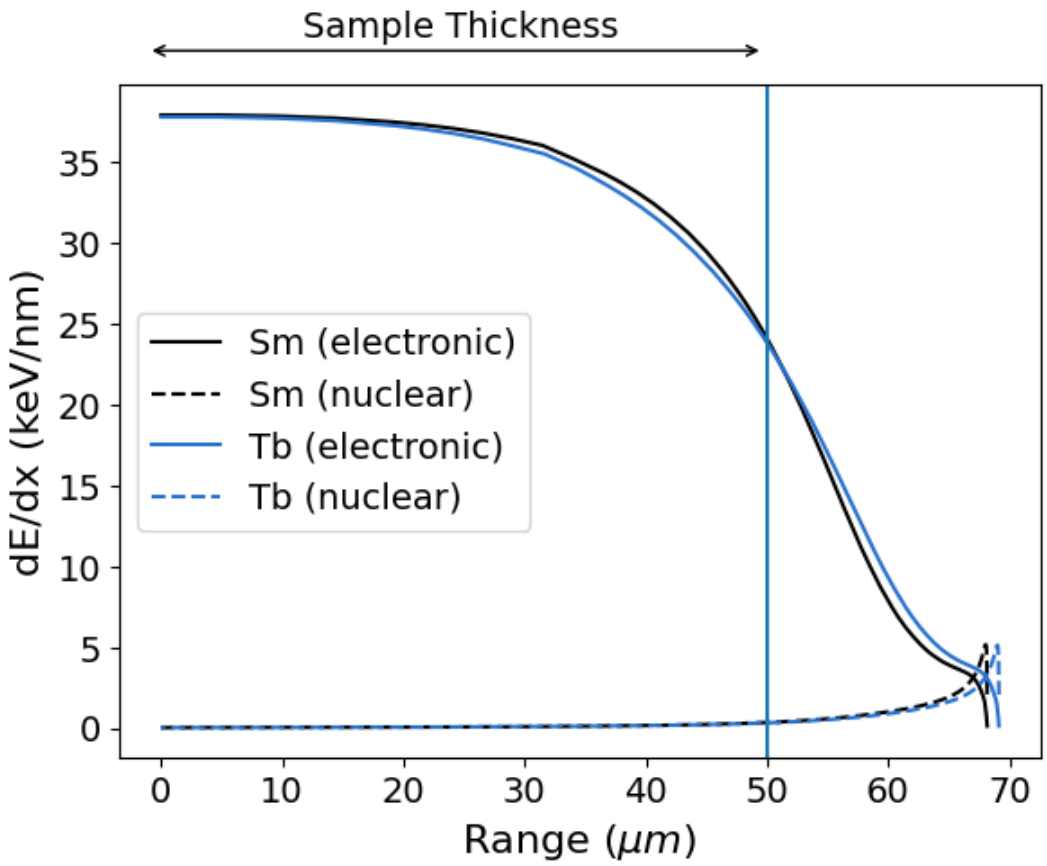

Figure 1: Evolution of the electronic stopping power of 1.1 GeV Au ions through the thickness of the irradiated REE phosphate samples ($SmPO_4$ and $TbPO_4$ with 50% theoretical densities of 2.78 and 2.84 g/cm^3, respectively); nuclear stopping power is negligible within the sample thickness.

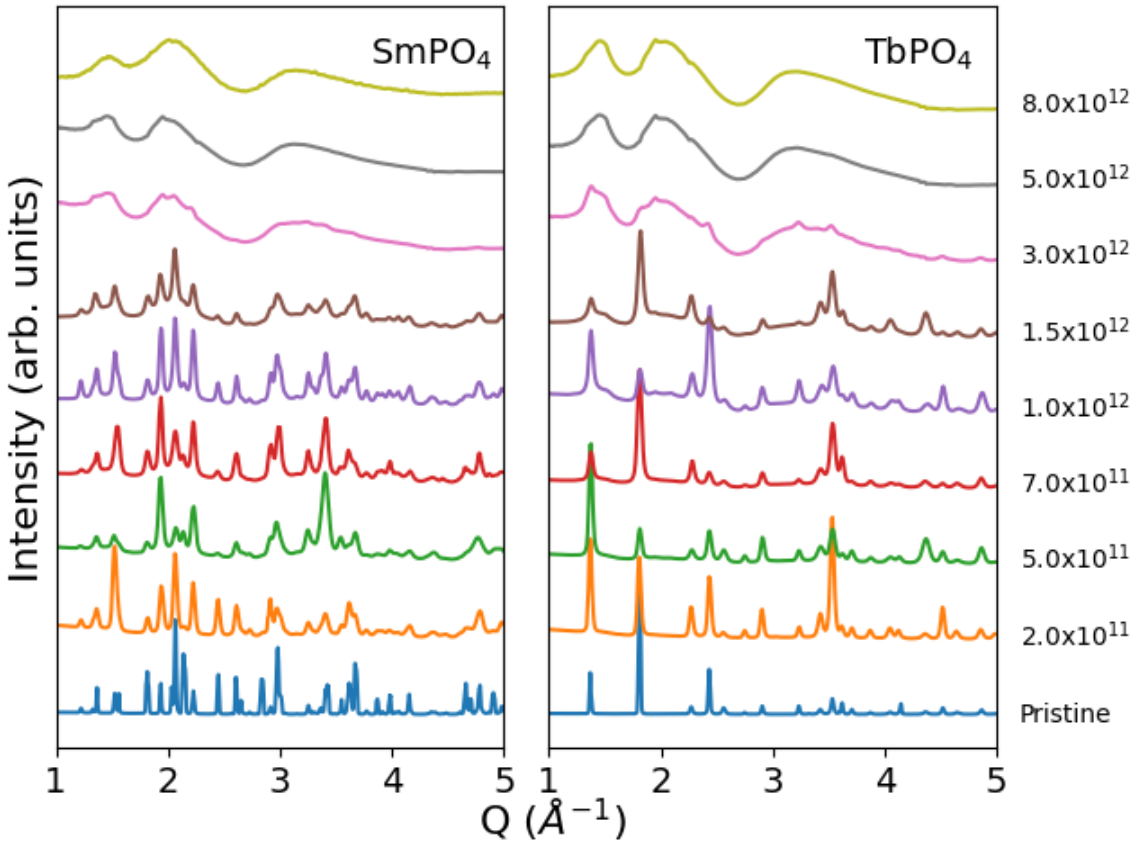

Figure 2: Selected synchrotron X-ray diffraction patterns of $SmPO_4$ (left) and $TbPO_4$ (right) irradiated with 1.1 GeV Au ions to various fluences (given in ions/cm^2).

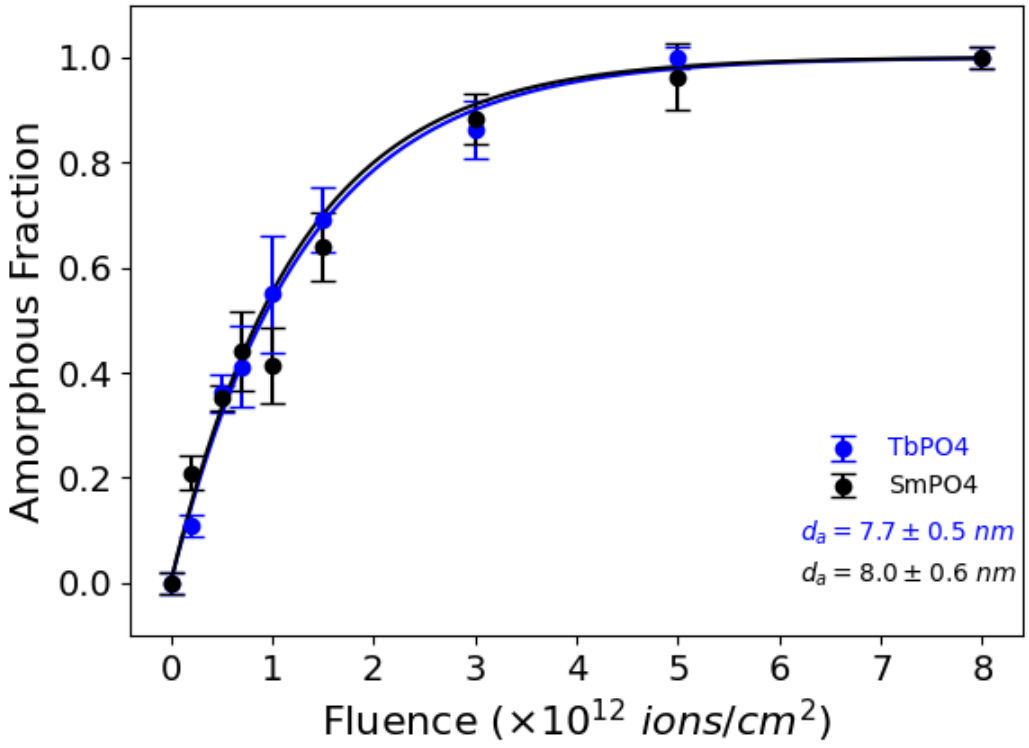

Figure 3: Amorphous fractions in $TbPO_4$ and $SmPO_4$ irradiated with swift heavy ions (1.1 GeV Au) from XRD diffraction analysis as a function of fluence. Single-impact fits (Equation 1) are shown as solid lines. Error bars represent the uncertainty in amorphous peak deconvolution. Amorphous track diameters (d_a) were calculated from cross-sections assuming cylindrical symmetry.

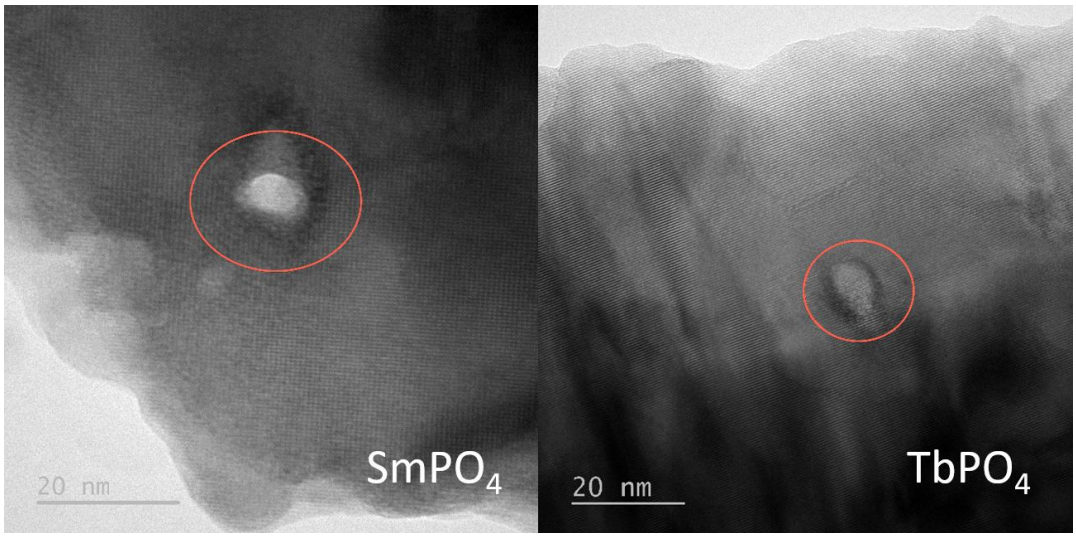

Figure 4: TEM images of ion tracks (circled in red) in irradiated $SmPO_4$ and $TbPO_4$. The ion tracks induced in both materials are fully amorphous with a similar size of about 8 nm in diameter.

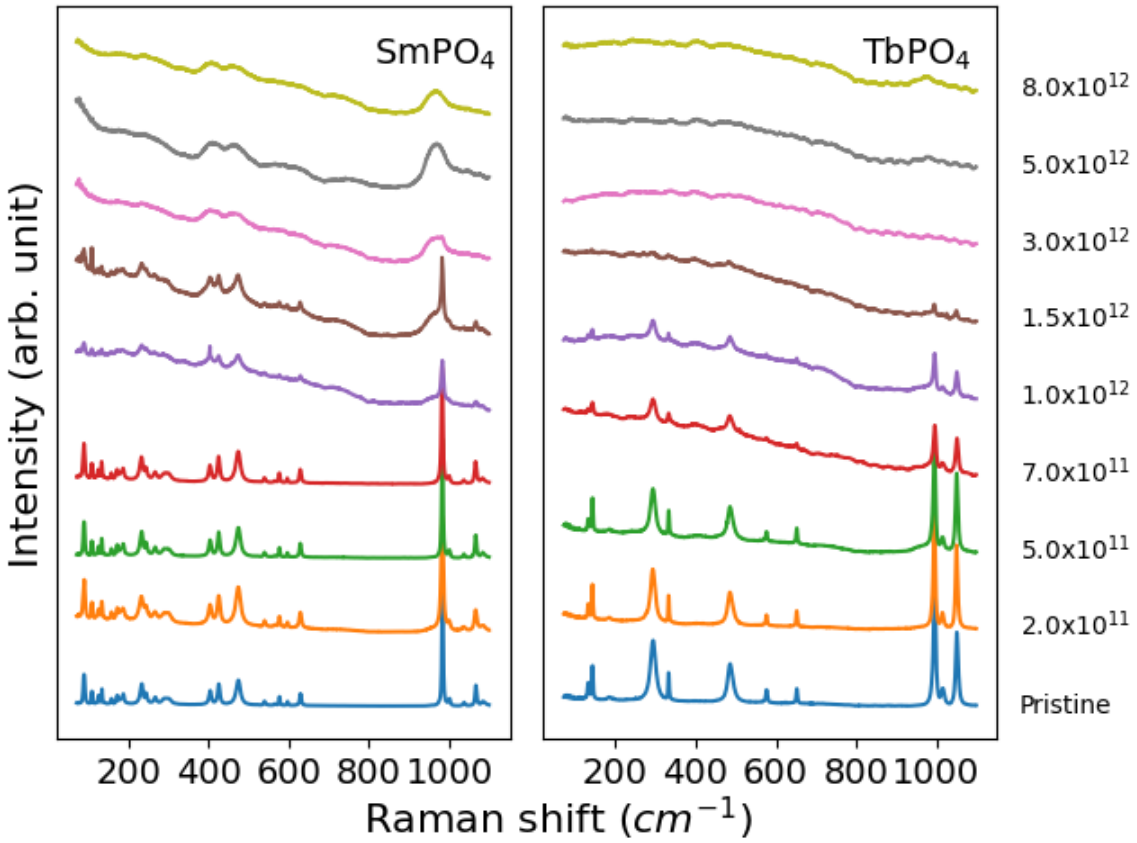

Figure 5: Selected Raman spectra for $SmPO_4$ (left) and $TbPO_4$ (right) irradiated with 1.1 GeV Au ions to various fluences (given in ions/cm^2).